ARTICLE IN PRESS

Journal of Advanced Research xxx (xxxx) xxx

Contents lists available at ScienceDirect

Journal of Advanced Research

journal homepage: www.elsevier.com/locate/jare

Design of highly leaf-adhesive and anti-UV herbicide nanoformulation for enhanced herbicidal activity

Dongdong Li [a,b,c], Jianan Li [d], Hao Li [b,c], Zhendong Bai [b,c], Chujian Ma [b,c], Haodong Bai [b,c], Dingfeng Luo [b,c], Zuren Li [a,b,c,*], Lianyang Bai [a,b,c,*]

[a] Longping Branch, College of Biology, Hunan University, Changsha 410125, China
[b] Yuelushan Laboratory, Changsha 410082, China
[c] Key Laboratory of Pesticide Assessment, Ministry of Agriculture and Rural Affairs, Hunan Academy of Agricultural Sciences, Changsha 410125, China
[d] College of Bioscience and Biotechnology, Hunan Agricultural University, Changsha 410125, China

HIGHLIGHTS

- TA-Fe complex-coated MSNs-NH_2 nano-carrier were established for herbicide delivery.
- The gained MSNs-TA-Fe nanohybrid could effectively protect CB from photodegradation.
- CB@MSNs-TA-Fe exhibited markedly enhanced surface wettability and foliar adhesion.
- CB@MSNs-TA-Fe showed superior control efficacy against barnyard grass.
- CB@MSNs-TA-Fe revealed excellent biosafety to rice, zebrafish, and earthworms.

GRAPHICAL ABSTRACT

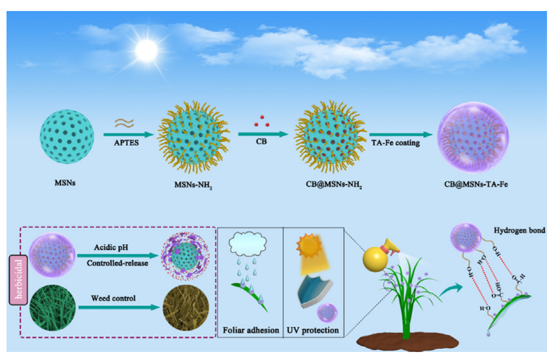

ARTICLE INFO

Article history:
Received 11 October 2024
Revised 8 December 2024
Accepted 21 December 2024
Available online xxxx

Keywords:
Nanoformulation
Foliar adhesion
Anti-UV property
Cyhalofop-butyl
Metal-phenolic film
Biosafety

ABSTRACT

Introduction: Conventional pesticide formulations have been widely used to boost agricultural productivity, but their weak foliar adhesion and instability under UV light during spraying lead to low utilization rates and potential environmental and health hazards. To counter these challenges, the development of nanoformulations represents a pivotal strategy. These advanced formulations are designed to enhance the efficacy of active ingredients (AIs) and reduce ecological impacts, thereby addressing the need for sustainable agricultural development.
Objectives: The study aims to fabricate a highly leaf-adhesive and anti-UV herbicide nanoformulation, designed to enhance the herbicidal activity and utilization rates of AIs.
Methods: Herein, the herbicide nanoformulations (Called CB@MSNs-TA-Fe) are synthesized by incorporating cyhalofop-butyl into tannic acid-Fe (III) ions-coated functionalized mesoporous silica. The foliar retention performance of the samples was assessed integrating SEM observation and HPLC analysis.
Results: The CB@MSNs-TA-Fe with rough outer surface displays typical core–shell structure featuring an average diameter of about 118 nm. After amino modification, the CB@MSNs-TA-Fe shows enhanced loading rate for CB (14.4 ± 0.2 %) and superior thermal stability. The release rate of CB within CB@MSNs-TA-Fe under acidic conditions is higher compared to that under alkaline and neutral conditions. Upon UV irradiation, the half-life of CB within CB@MSNs-TA-Fe nanoparticles is 12.4 times higher than that of CB technical (CB TC). Enhanced foliar adhesion of CB@MSNs-TA-Fe on hydrophobic leaf surfaces is observed, which can effectively mitigate the risk of wash-off by rainfall. The CB@MSNs-TA-Fe displays enhanced

* Corresponding authors.
E-mail addresses: lizuren88214@hunaas.cn (Z. Li), lybai@hunaas.cn (L. Bai).

https://doi.org/10.1016/j.jare.2024.12.034

Please cite this article as: D. Li, J. Li, H. Li et al., Design of highly leaf-adhesive and anti-UV herbicide nanoformulation for enhanced herbicidal activity, Journal of Advanced Research, https://doi.org/10.1016/j.jare.2024.12.034

herbicidal efficacies against barnyard grass under UV irradiation or simulated rainwater scouring, compared with CB TC and CB oil dispersion. Furthermore, the TA-Fe-coated $MSNs-NH_2$ nano-carrier (MSNs-TA-Fe) reveals excellent biosafety on rice, zebrafish, and earthworms.

Conclusion: The developed TA-Fe-functionalized herbicide nanoformulations, with high foliar adhesion and anti-UV properties, effectively improve the utilization efficiency of AIs, thus offering innovative solutions for the development of efficient pesticide formulations.

Introduction

Herbicides serve as a valuable tool for weed management, offering convenience, cost-effectiveness, and practicality. However, conventional herbicide formulations often suffer from low utilization efficiency, primarily due to photolysis [1], inadequate foliar adhesion [2], and rain-induced wash-off [3] during agricultural application. These limitations necessitate excessive applications to achieve satisfactory herbicidal effects, resulting in long-term overuse and abuse of herbicides, which negatively affect the environment and human health [4]. In this scenario, developing a highly efficient herbicide formulation with enhanced adhesion and anti-UV properties is particularly necessary and urgent.

Herbicide nanoformulations are highly desirable formulations for reducing the usage of AIs while concurrently improving their utilization efficiency. More specifically, herbicide nanoformulations can enhance the photostability of AIs, ameliorate their flush-resistance performance, and significantly augment their adhesion and retention on plant foliage [5,6]. Further, leveraging their small size effect, the herbicide nanoformulations efficiently penetrate weed leaves and stems, thereby enhancing the accumulation of effective concentrations within the weeds and augmenting herbicidal efficacy [6,7]. He et al. [8] found that the developed quizalofop-p-ethyl@carboxyl hollow mesoporous silica@copper-benzene-1,4-dicarboxylate metal organic framework (QE@HMS@Cu-BDC) nanoparticles, approximately 140 nm in size, can more efficiently enter plant leaves and stems. Their small size enhances the transport of the active ingredients (AIs) throughout the plant, potentially improving herbicidal activity. Nano-carriers play a pivotal role in the development of herbicide nanoformulations [6,9,10]. Currently, the fabrication of these nanoformulations commonly employs mesoporous silica nanoparticles (MSNs) [8], carbon nanoparticles [11], and covalent organic frameworks [6] as nano-carrier. Dong et al. [11]developed nanoformulations based on chitosan-gated porous carbon nanoparticles for the delivery of paraquat (PQ). The as-prepared nanoformulations greatly improve the efficacy and safety of agrochemical delivery, ensuring the optimal utilization efficiency of the AIs. Zhao et al. [12] reported the successful encapsulation of quinclorac (QNC) in ethidium-bromide-based covalent organic frameworks (EB-COFs) nanosheets, constructing the herbicide nanoformulations QNC@EB-COFs through mechanical delamination. The QNC@EB-COFs exhibited a notably high QNC loading capacity of 41 % (w/w) and demonstrated outstanding herbicidal efficacy against barnyard grass. Although these carriers can fulfill the need for herbicide loading and strengthen the utilization rates of herbicides to some extent, their fabrication is often hindered by issues such as complex operational process, prolonged synthesis times, high production costs, and demanding reaction conditions, significantly impeding their practical application in agriculture. Conversely, MSNs offer distinct benefits, including simple synthesis procedure, robust stability, and facile surface functionalization [13]. These attributes highlight the potential of MSNs as nanocarriers in herbicide nanoformulations.

Applying functional coatings to nano-carrier surfaces can markedly enhance the photostability of AIs and the adhesion of nanocarrier to hydrophobic leaves. This strategy is of great significance for improving the effective utilization rate of AIs. Tannic acid (TA), a plant-derived natural polyphenol, demonstrates strong light absorption in the ultraviolet spectrum, thereby protecting AIs from UV light degradation [5,14,15]. For instance, Teng et al. [5] found that the photostability enhancement of pesticides had close association with the pronounced UV absorption of TA at the maximum absorption wavelength of pesticide. Moreover, the molecular structure of TA is rich in galloyl groups, which can coordinate with iron ions to form metal-phenolic networks on the surface of nanomaterials under mildly alkaline conditions [16–18]. These galloyl groups interact with the fatty alcohols, acids, and aldehydes of the leaf's wax layer via hydrogen bonding, which significantly enhances the wettability, affinity and adhesion of nano-carrier to the leaf surface [19–21].

Rice, a crucial global alimentary crop, feeds over half of the Earth's population [22,23]. The presence of weeds in rice fields, which are challenging to eradicate, poses a significant threat to rice production due to their competitive interaction with rice crops. This competition can lead to a substantial decrease in rice yields, potentially resulting in a worldwide loss of 10–35 % [24]. Barnyard grass is recognized as one of the top ten most pernicious weeds globally and is considered the most detrimental to rice growth worldwide [25,26]. Cyhalofop-butyl (CB), an oxyphenoxypropionic acid herbicide characterized by its internal absorption and conduction, is extensively utilized for the control of barnyard grasses (*Echinochloa crus-galli*) in paddy rice fields [27]. The hydrophobic waxy layer of barnyard grass leaves hinders the efficient deposition of the sprayed CB onto their target surface, thereby contributing to a high off-target rate [28,29]. Furthermore, commercial CB formulations, with micrometer size, are prone to slipping off leaf surfaces, leading to the loss of AIs and low utilization rates in field applications [1,6]. Moreover, Zhu et al. [30] reported that, under UV light irradiation, the photodegradation half-life ($t_{1/2}$) of CB technical (CB TC) in both buffer solution (pH = 5.0) and deionized water (pH = 6.8) was less than 5 min. This demonstrates the instability of CB under UV light, which could potentially compromise its control efficacy upon exposure to sunlight. In this scenario, a highly leaf-adhesive and anti-UV formulation should be developed to improve the CB utilization efficiency.

Herein, metal-phenolic networks constructed based on TA and Fe^{3+} are coated on the CB-loaded $MSNs-NH_2$ nanoparticles ($CB@MSNs-NH_2$) surface to fabricate a highly leaf-adhesive and anti-UV herbicide nanoformulations (CB@MSNs-TA-Fe) for effective weed control (Scheme 1). Notably, the TA-Fe coating on the $CB@MSNs-NH_2$ surface not only protects CB from UV degradation and as a protective barrier avoids premature release of CB, but also enhances aqueous droplet spreadability on barnyard grass blades because of its improved surface wettability. Moreover, polyphenol groups of TA form hydrogen bonds with the groups of waxy layers, which enables CB@MSNs-TA-Fe with significantly improved foliar adhesion and flush-resistance performance on hydrophobic blades,

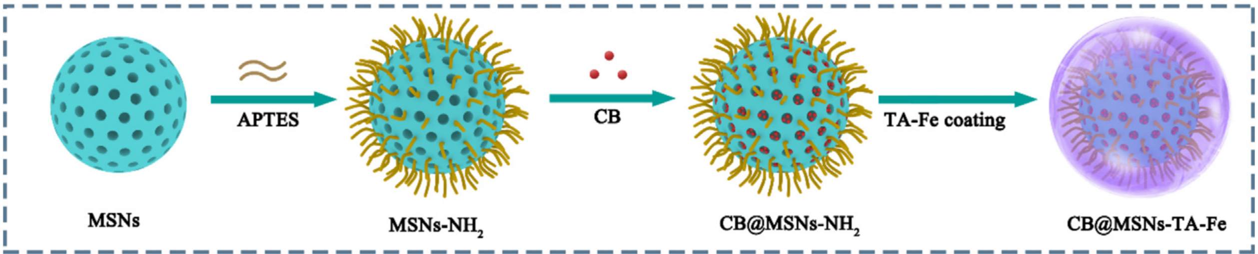

Scheme 1. Schematic diagram of the synthesis of CB@MSNs-TA-Fe.

thereby effectively boosting the utilization efficiency of the AIs. The CB@MSNs-TA-Fe shows higher herbicidal activity against barnyard grass than CB TC and CB oil dispersion (CB OD) under UV irradiation or simulated rainwater scouring. The TA-Fe-coated MSNs-NH_2 (MSNs-TA-Fe) nano-carrier is demonstrated to be biosafe for rice, zebrafish (Danio rerio) and earthworm (*Eisenia fetida*). Overall, this work provides an essential reference for fabricating highly leaf-adhesive and anti-UV herbicide nanoformulations aimed at improving the utilization efficiency of CB, thereby offering innovative solutions for sustainable agricultural development.

Results and discussion

Materials characterization

Scheme 1 illustrates the detailed synthesis process for CB@MSNs-TA-Fe nanoparticles. Initially, the MSNs nanoparticle was synthesized via the sol–gel method [31]. Cetyltrimethylammonium chloride (CTAC) served as a templating agent, while tetraethyl orthosilicate was used as the silicon source. Following the removal of CTAC from the pores structure of MSNs, the resultant MSNs were subjected to amination using 3-Aminopropyltriethoxysilane (APTES), thereby conferring the synthesis of MSNs-NH_2. Then, the CB molecules were encapsulated within the MSNs-NH_2 pores by physisorption to prepare the CB@MSNs-NH_2 nanoparticles. Ultimately, the formed TA–Fe metal–phenolic network was deposited on the CB@MSNs-NH_2 surface via the coordination between TA and Fe^{3+} ions, yielding the CB@MSNs-TA-Fe nanoparticles endowed with high foliar adhesion and anti-UV properties [32].

The hydrodynamic sizes of the fabricated nanoparticles are ascertained utilizing dynamic light scattering. As illustrated in **Fig. S1**A, the MSNs-NH_2 nanoparticles demonstrate an average hydrodynamic size of 155 ± 0.6 nm in aqueous medium. By contrast, the synthesized CB@MSNs-TA-Fe has an augmented average diameter of 181 ± 0.5 nm, likely indicative of the deposition of the TA-Fe complex on the nanoparticle surface. **Fig. S1**B clearly delineates that MSNs-NH_2 and CB@MSNs-TA-Fe display a narrow particle size distribution, indicative of their uniformity in size. The polydispersity index (PDI), a metric frequently employed to assess particle aggregation [33], is determined for MSN-NH_2 and CB@MSNs-TA-Fe, yielding PDI values of 0.13 ± 0.009 and 0.17 ± 0.015, respectively. Both indices, being below 0.2, are suggestive of their exceptional dispersibility in water.

Transmission electron microscope (TEM) was utilized to further explore the microstructure of MSNs-NH_2 (Fig. 1**A**) and CB@MSNs-TA-Fe (Fig. 1**B**). The MSNs-NH_2 nanoparticles depict uniformly spherical morphology featuring an average diameter of about 103 nm. Additionally, their porous structure is distinctly observable in the TEM image. The TA-Fe coating leads to an increase in the average diameter of the CB@MSNs-TA-Fe nanoparticles to approximately 118 nm, accompanied by a discernible surface roughness. Notably, a thin shell is clearly discernible on the CB@MSNs-TA-Fe nanoparticles surface, producing a distinct core–shell architecture with an estimated shell thickness of 15 nm (Fig. 1**B**). These results further corroborate the successful coating of TA-Fe film on the MSNs-NH_2 nanoparticles. The energy dispersive spectrometer (EDS) spectrum (**Fig. S2**) confirms the presence of Si, O, N, F, and Fe elements within the CB@MSNs-TA-Fe nanoparticles. The energy dispersive Xray (EDX) mapping images (Fig. 1**C**-I) reveal that Si and O elements are attributable to the MSNs component. The distribution area of N and F elements corresponds with the profile of the CB@MSNs-TA-Fe nanoparticles, which likely affirms the successful amino modification and encapsulation of CB molecules within the MSNs-NH_2. The elemental mapping of Fe exhibits a similar distribution pattern, further proving the formation of a TA-Fe film on the CB@MSNs-NH_2 surface.

The porous structure of samples was further characterized using the Brunauer Emmett Teller (BET) analysis method [34,35]. The N_2 adsorption–desorption measurement results (**Fig. S3** and **Table S1,** Supporting information) verify the mesoporous structure and large cavities of the MSNs and MSNs-NH_2 carriers with porous properties. These characteristics provide ample channels for pesticide loading, rendering them as optimal carriers for the construction of various pesticide delivery systems. Combined with the average pore size (7.51 nm) of MSNs-NH_2 (**Table S1**), the 3D size of CB molecule is calculated to be 1.83 × 0.97 × 0.77 nm (**Fig. S4**); thus, CB could be easily loaded into the mesopores channels of the MSNs-NH_2 nanoparticles in theory. Throughout the synthesis of the CB@MSNs-TA-Fe samples, the BET surface area values exhibit a certain amount of gradual decline, indicative of the successful progression of each modification step. As shown in **Table S1**, the pore volume of pristine MSNs (0.929 $cm^3 \cdot g^{-1}$) decreases to 0.711 $cm^3 \cdot g^{-1}$ post-amino modification to form MSNs-NH_2. Upon loading with CB, the pore volume lowers to 0.199 cm^3 g^{-1} in the CB@MSNs-NH_2 and further to 0.184 $cm^3 \cdot g^{-1}$ following the TA-Fe modification. These sequential reductions in pore volume corroborate the successful fabrication of the CB@MSNs-TA-Fe composite.

Zeta potential analysis was employed to study the surface modification processes.

Fig. 2**A** illustrates that the zeta potential of pristine MSNs was −29.0 mV, attributed to the presence of silanol groups on their surface [36]. Following amino functionalization with APTES, the zeta potential of MSNs-NH_2 increases to + 23.8 mV, ascribed to the positive charge of amino groups [36]. The loading of CB leads to a slight reduction in zeta potential to + 15.9 mV for CB@MSNs-NH_2. Significantly, the ζ-potential of CB TC is negative, which is opposite to the positive ζ-potential for MSNs-NH_2. Consequently, more CB molecules can be adsorbed onto the MSNs-NH_2 surface via electrostatic interactions, conferring upon MSNs-NH_2 an elevated loading capacity for CB. Surface modification of CB@MSNs-NH_2 nanoparticles with TA (CB@MSNs-TA) induces a further decrease in zeta potential, yielding a value of −17.7 mV, likely due to the negative charges of TA resulting from phenolic hydroxyl and carboxyl groups [37]. With the introduction of Fe^{3+} ions, the

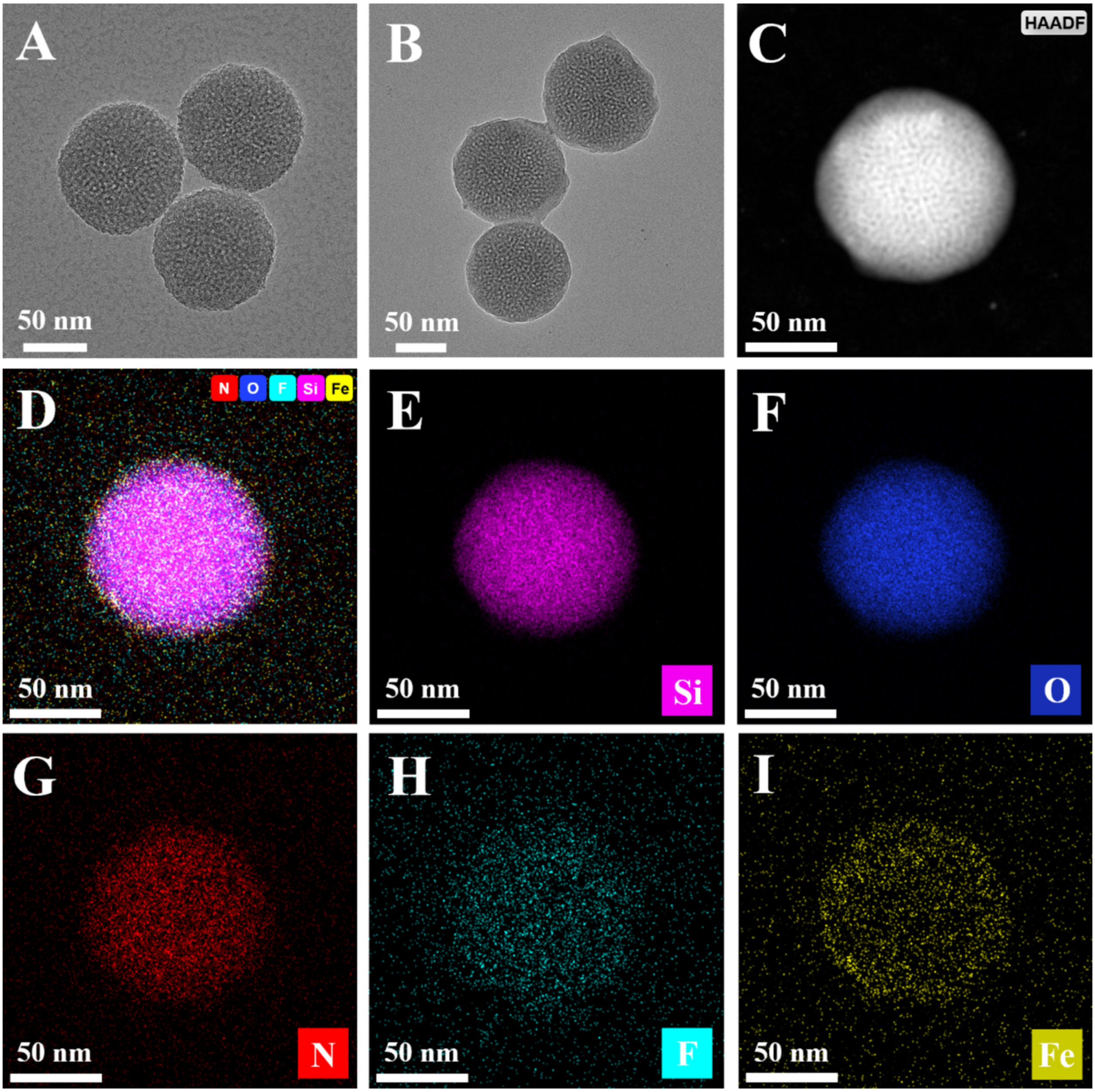

Fig. 1. Morphology characterization of MSNs-NH_2 and CB@MSNs-TA-Fe. (A) TEM images of MSNs-NH_2 . (B) TEM images of CB@MSNs-TA-Fe. (C-I) EDX mapping images corresponding to Si, O, N, F, Fe elements of CB@MSNs-TA-Fe.

zeta potential value of CB@MSNs-TA-Fe increases to −6.8 mV, further substantiating the successful coating of TA-Fe film on the nanoparticles surface.

The functional groups in samples were analyzed using Fourier transform infrared spectroscopy (FTIR). As depicted in Fig. 2**B**, CB TC displays distinctive absorption bands at 2873–2960, 2226, and 1731 cm^{-1}, corresponding to the stretching vibrations of the methyl group (CH_3), cyano group (C≡N), and carbonyl group (C = O), respectively [6]. Besides, MSNs show three prominent characteristic bands at 437, 806, and 1058 cm^{-1}, which are indicative of the O-Si-O bending vibration, Si-O bending vibration, and Si-O-Si stretching vibration, respectively [38,39]. The post-modification with APTES introduces a novel absorption peak at 1563 cm^{-1}, attributed to the bending vibration of N–H bonds, thereby signifying the successful amino functionalization [40]. The FTIR spectrum of CB@MSNs-NH_2 reveals the concurrent presence of characteristic peaks for both CB and MSNs-NH_2, further validating the successful loading of CB into MSNs-NH_2 nanoparticles. In comparison to MSNs-NH_2, two new peaks at 1734 and 1191 cm^{-1} are found in the FTIR spectra of MSNs-TA-Fe, corresponding to the C = O and C – OH stretching vibration of TA, respectively, confirming the successful modification of TA [20].

The elemental composition of the nanoparticle surface was further analyzed by X-ray photoelectron spectroscopy (XPS). As depicted in Fig. 2**C**, the XPS spectrum of MSNs-NH_2 shows pronounced O1 s and Si 2p peaks at 532.5 eV and 102.9 eV, respectively, corresponding to the characteristic element of MSNs. Moreover, the presence of N1 s peaks at 399.0 eV substantiates the successful amino modification on the MSNs surface. Compared with MSNs-NH_2, the CB@MSNs-TA-Fe spectrum in Fig. 2**C** reveals two new distinctive peaks corresponding to F1 s and Fe 2p at 689.0 and 711.5 eV, respectively. These results firmly prove the successful loading of CB and coating of the TA-Fe on the CB@MSNs-NH_2 surface, corresponding well with the EDS data.

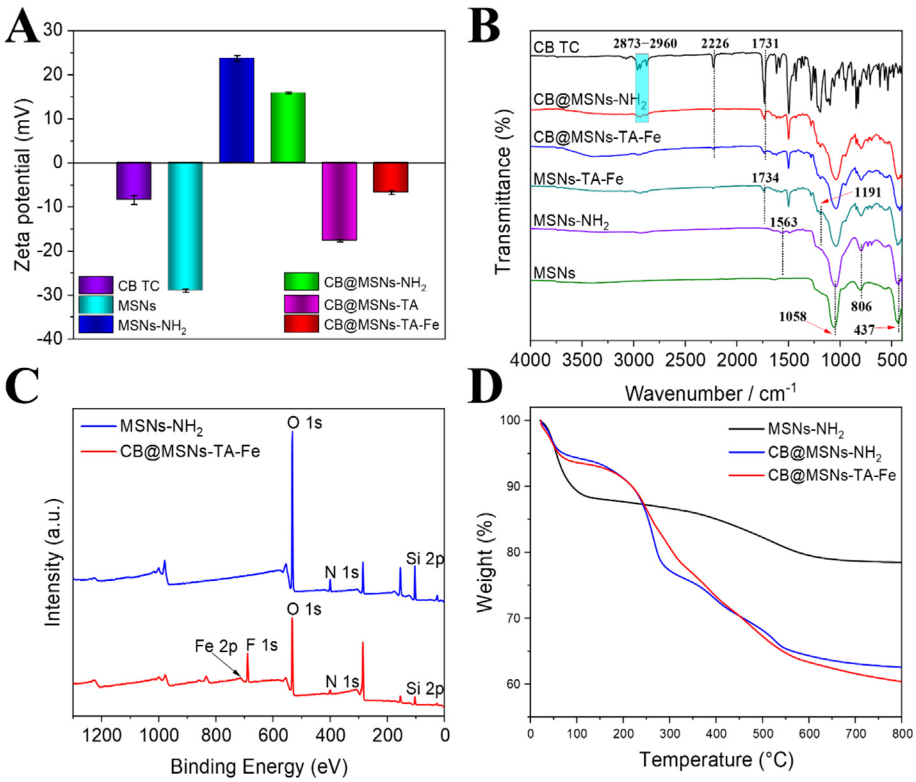

Fig. 2. Physicochemical characterization of diverse samples. (A) Zeta potential of CB TC, MSNs, $MSNs-NH_2$, $CB@MSNs-NH_2$, CB@MSNs-TA, CB@MSNs-TA-Fe. (B) FTIR spectra of CB TC, MSNs, $MSNs-NH_2$, $CB@MSNs-NH_2$, MSNs-TA-Fe, CB@MSNs-TA-Fe. (C) XPS spectra of $MSNs-NH_2$ and CB@MSNs-TA-Fe. (D) TGA curves of $MSNs-NH_2$, $CB@MSNs-NH_2$, and CB@MSNs-TA-Fe.

Noteworthily, the weak intensity of the Fe 2p peak in the XPS spectrum suggests that the TA-Fe coating is a thin layer, a feature highly congruent with the TEM analysis.

Fig. 2**D** illustrates the thermogravimetric analyzer (TGA) curves of $MSNs-NH_2$, $CB@MSNs-NH_2$, and CB@MSNs-TA-Fe. As shown here, the $MSNs-NH_2$ exhibits a final weight loss of 21.54 %, attributed to water evaporation and the thermal decomposition of organic functional groups [41]. In contrast, $CB@MSNs-NH_2$ demonstrates an elevated mass loss of 37.47 %, suggesting an approximate CB loading of 15.93 % into $MSNs-NH_2$. This result is highly consistent with the pesticide loading rate determined by high-performance liquid chromatography (HPLC) (**Fig. S5**). Furthermore, the CB@MSNs-TA-Fe displays a further augmented weight loss of 39.69 wt%. Combined with the above characterization results, they collectively substantiate the successful coating of the TA-Fe complex on the $CB@MSNs-NH_2$ surface.

Pesticide loading and release analysis

Fig. S5 illustrates the loading rates of various CB formulations. Noteworthily, the loading rate of $CB@MSNs-NH_2$ reaches 15.0 ± 1. 0 %, significantly surpassing that of CB@MSNs at 9.9 ± 0.6 %. Combined with the zeta potential results, the elevated loading rate of $CB@MSNs-NH_2$ can be attributed to the positive surface charge of $MSNs-NH_2$, which facilitates the adsorption of negatively charged CB molecules through electrostatic interactions. Nevertheless, this loading rate is slightly reduced to 14.4 ± 0.2 % after the coating of TA-Fe film, potentially due to pesticide leakage during the coating process. Additionally, the release behaviors of CB from CB@MSNs-TA-Fe were investigated under different pH values using the dialysis bag method. The detailed procedure is outlined in the supporting information (SI).

Stability of CB@MSNs-TA-Fe nanoparticles

It has been reported that CB is prone to photodegradation under UV irradiation, significantly reducing its efficacy in weed control [6,30]. As illustrated in Fig. 3**A**, the residual rate of CB TC plummets to a mere 7.0 % after 25 min, reflecting the inherent instability of CB molecules to UV radiation. By contrast, the CB encapsulated within $CB@MSNs-NH_2$ nanoparticles exhibits a residual ratio of 67.2 %. Furthermore, applying the TA-Fe coating on $CB@MSNs-NH_2$ nanoparticles significantly bolsters the photostability of CB, with the residual ratio remaining at 80.0 % of the original value. Zhao et al. reported similar findings while utilizing spherical COF for the loading of CB [6]. This improvement in photostability can effectively reduce the application dosage of the herbicide while maintaining its good herbicidal effect, thus leading to an improved utilization efficiency of AIs. The underlying mechanism for this photostability improvement is ascribed to the absorption characteristics of TA-Fe. At the maximum absorption wavelength of CB TC (233 nm), TA-Fe exhibits a pronounced absorption peak intensity (Fig. 3**B**), indicating its capacity to shield CB from photodegradation through the absorption and reflection of UV radiation [5]. The photodegradation data is found to conform closely to the first-order kinetic model, as depicted in Fig. 3**C** and Table 1, following the equation $\ln(C_t/C_0) = -kt$. The respective photodegradation rate constants for CB TC, $CB@MSNs-NH_2$, and CB@MSNs-TA-Fe are determined to be 0.105, 0.010, and 0.007 min^{-1}. Strikingly, the photodegradation half-life of CB encapsulated within CB@MSNs-TA-Fe (88.0 min) is 12.4 times higher than that of CB TC (7.1 min). Consequently, the MSNs-TA-Fe nanocomposite would be an ideal carrier that can markedly augment the photostability of AIs. Pesticide formulations, subjected to the complexities of environmental conditions during storage and transportation, are

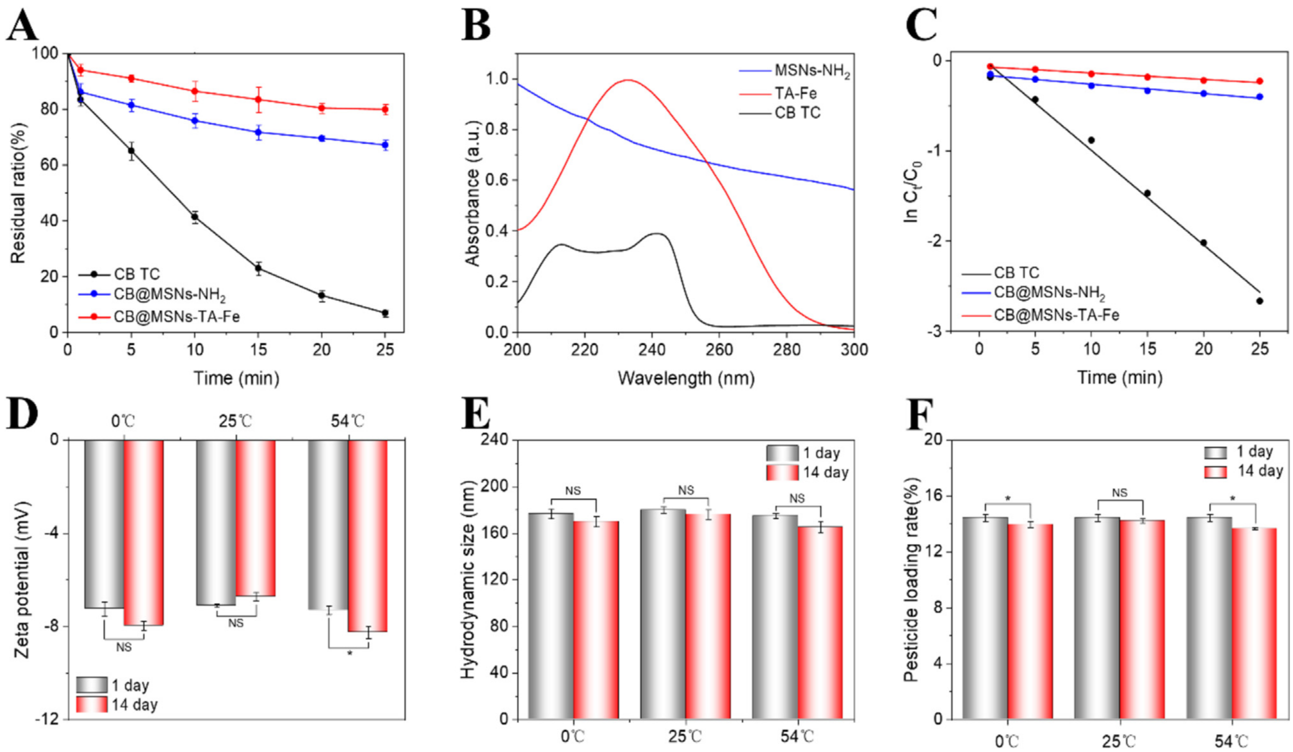

Fig. 3. Strong anti-UV properties and superior thermal stability of CB@MSNs-TA-Fe nanoparticles. (A) Photostability of CB, CB@MSNs-NH_2 , and CB@MSNs-TA-Fe under UV irradiation. (B) UV–vis absorption spectra of MSNs-NH_2 , TA-Fe, and CB TC. (C) First-order models of CB photodegradation for CB TC, CB@MSNs-NH_2 and CB@MSNs-TA-Fe. (D) Zeta potential, (E) hydrodynamic sizes and (F) pesticide loading rate changes of CB@MSNs-TA-Fe at 0, 25, 54℃ for 14 days. Data were expressed as mean ± standard error of the mean (SE) for all experiments. An asterisk (*) indicates a statistically significant difference ($P < 0.05$). NS denotes an insignificant difference.

Table 1
Modeling parameters for photodegradation of CB TC, CB@MSNs-NH_2, and CB@MSNs-TA-Fe under UV irradiation.

Parameter	First-order kinetics		
	CB TC	CB@MSNs-NH_2	CB@MSNs-TA-Fe
K (min^{-1})	0.105	0.010	0.007
R^2	0.988	0.965	0.955
DT_{50} (min)	7.1	51.7	88.0

prone to the volatilization of AIs, presenting potential risks to human health. Hence, the stability of CB@MSNs-TA-Fe was assessed over14 days at varying temperatures, with evaluations focused on changes in pesticide loading rate, zeta potential, and hydrodynamic sizes. As illustrated in Fig. 3**D and E**, the zeta potential and hydrodynamic sizes of CB@MSNs-TA-Fe exhibit minimal variation at various temperatures, attesting to its remarkable stability in storage conditions. Concurrently, the decomposition rates of CB within CB@MSNs-TA-Fe after 14 days are only 3.31 %, 1.60 %, and 5.33 % for storage at 0 °C, 25 °C, and 54 °C, respectively (Fig. 3**F**). These results indicate negligible degradation of CB, substantiating its exceptional stability. Collectively, the robust stability profile of CB@MSNs-TA-Fe strongly supports its viability for application in agricultural settings.

Wettability of foliage and adhesion mechanism

The wettability and adhesion of pesticide formulations on foliar surfaces are pivotal to enhancing the utilization efficiency of AIs. The surface wettability of CB@MSNs-TA-Fe on barnyard grass leaves was assessed by contact angle measurements. As depicted in Fig. 4**A**, the contact angle is reduced to 81.3 ± 1.3° following TA-Fe modification, a result that corresponds with the findings reported in the literature [42]. This reduction signifies a significant enhancement in the wettability and leaf affinity of the CB@MSNs-TA-Fe nanoparticles. Scanning electron microscope (SEM) imaging can more visually observe the retention state and flush-resistance performance of prepared nanoparticles on leaves. Numerous irregular protrusions, folds, and stomata were observed on the leaf surface of barnyard grass (Fig. 4**B**), creating micro/nanostructures with sufficient roughness to provide abundant sites for pesticide attachment. Prior to water rinsing, an abundance of particles is observed on the leaves treated with various sample suspensions. After washing with deionized water, only a small quantity of particles remains on the leaves treated with CB TC. In contrast, a greater retention of particles is observed on leaves treated with CB@MSNs-NH_2 and CB@MSNs-TA-Fe, especially the CB@MSNs-TA-Fe. These results suggest that CB@MSNs-TA-Fe can effectively resist rain erosion without rolling off and facilitate the foliar deposition of pesticide droplets, thereby substantially improving the utilization rate of AIs. To further quantify the foliar retention of CB@MSNs-TA-Fe nanoparticles with greater precision, a simulated rainwater washing experiment was conducted. The results were subsequently analyzed using HPLC (Fig. 4**C**). After rinsing with simulated rainwater, the retention rate of CB@MSNs-NH_2 on barnyard grass leaves is measured at 64.7 ± 3.4 %, which is estimated to be 1.7 times higher than that of CB TC. This phenomenon may be ascribed to the expanded contact area between the foliar surface and the spherical carrier with high specific surface area and superior dispersion [43]. After the coating of TA-Fe film, the retention rate of CB@MSNs-TA-Fe is further elevated to 81.4 ± 3.3 %, corresponding well with the SEM analysis. This suggests that the TA-Fe metal-polyphenol network on the nanoparticles surface substantially contributes to foliar adhesion and retention. The enhanced foliar adhesion of CB@MSNs-TA-Fe is ascribed to the hydrogen bonding between the catechol groups present in TA

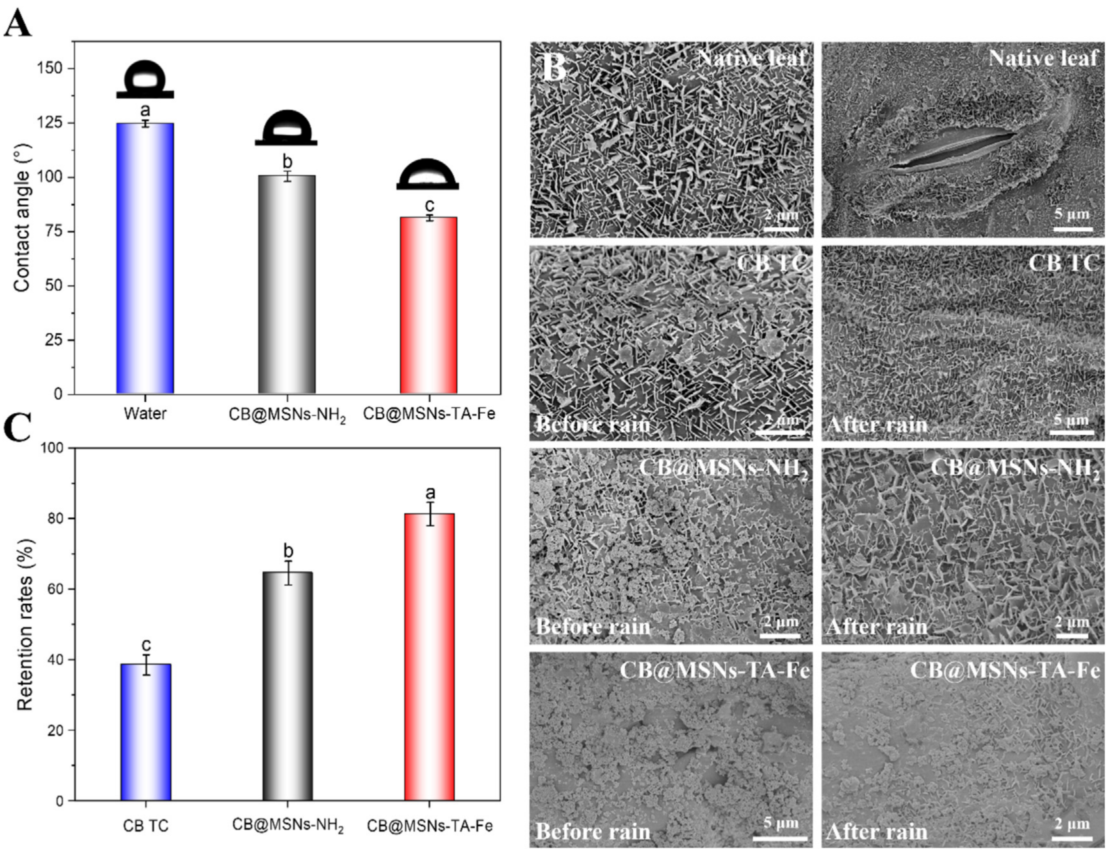

Fig. 4. Excellent surface wettability and high foliar adhesion of CB@MSNs-TA-Fe on hydrophobic blades. (A) Contact angles of CB@MSNs-NH_2 and CB@MSNs-TA-Fe on barnyard grass leaves. (B) SEM images of barnyard grass leaves and leaves treated with CB, CB@MSNs-NH_2 , and CB@MSNs-TA-Fe before and after washing. (C) The retention rates (I/I_0) of CB@MSNs-TA-Fe relative to CB TC and CB@MSNs-NH_2 on barnyard grass leaves after washing. Data were expressed as mean ± standard error of the mean (SE) for all experiments. Different lowercase letters indicate statistically significant differences ($P \leq 0.05$).

and the lipid components, including fatty alcohols, acids, and aldehydes of the leafs' wax layer [19]. These results are in accordance with previous reports on polyphenol adhesive chemistry [19]. Maintaining the nanoformulations on the waxy epidermis of leaves and resisting rain erosion can significantly improve the exposure and uptake of AIs by weeds. Consequently, it becomes feasible to use a lower dosage of the herbicide while maintaining superior herbicidal effect.

Herbicidal activity of CB@MSNs-TA-Fe against barnyard grass

The ultraviolet protection efficacy of CB@MSNs-TA-Fe was assessed. Fig. 5**A** (a-d) illustrates a significant improvement in herbicidal activity for CB@MSNs-TA-Fe following UV exposure compared to CB TC and CB OD. The dose- and time-dependent fresh weight inhibitions are presented in Fig. 5**B**. After 14 days of application, the control efficacy of CB@MSNs-TA-Fe reaches 87.8 %-92.0 %, markedly exceeding that of CB TC (66.6 %-74.1 %) and CB OD (75.1 %-82.5 %). These findings indicate that CB@MSNs-TA-Fe significantly improves the photostability of CB to UV radiation through the UV absorption and shielding properties of the TA-Fe coating, thus maintaining superior herbicidal efficacy post-UV irradiation. Moreover, the flush-resistance performance of CB@MSNs-TA-Fe after simulated rainwater was explored. As illustrated in Fig. 5**A** (e-h), barnyard grass treated with tween solution displays normal growth over the 14-day growing period. By contrast, weeds treated with CB@MSNs-TA-Fe suspensions demonstrate a significantly enhanced herbicidal effect at a dosage of 50 $\mu g \cdot mL^{-1}$ of AIs, outperforming those treated with CB OD and CB TC. This result aligns with the fresh weight inhibition data in Fig. 5**C**, which highlights the superior flush-resistance performance and decent herbicidal efficacy of CB@MSNs-TA-Fe following simulated rainwater washing. Collectively, these results suggest that CB@MSNs-TA-Fe can effectively control the emergence and spread of malignant weeds, primarily ascribed to the enhanced photostability and foliar adhesion of CB.

Biosafety evaluation of MSNs-TA-Fe nanoparticles

A safety experiment on rice seedlings was performed to investigate the safety and feasibility of using MSNs-TA-Fe in paddy fields. As shown in **Fig. S7**, MSNs-TA-Fe exhibits negligible phytotoxic effects across all concentrations, demonstrating no detrimental impact on rice seedling growth. Seven days after foliar treatment, no significant differences are observed in the stem length, root length, fresh weight, and SPAD value between the MSNs-TA-Fe treated groups and the control at various concentrations, as presented in Fig. 6. The results collectively confirm the nano-carrier MSNs-TA-Fe to be non-toxic to rice growth. Consequently, the MSNs-TA-Fe is deemed a biocompatible nano-carrier candidate suitable for herbicide nanoformulations. Following the delivery of the pesticide, the carrier material (MSNs-TA-Fe) remains in the environment, with Fe and Si elements potentially being released during its degradation. Therefore, the biosafety of MSNs-TA-Fe as a pesticide carrier should be a subject of increased concern in practical application. In this study, the potential toxicity of MSNs-TA-Fe nanoparticles at the level of aquatic organisms was

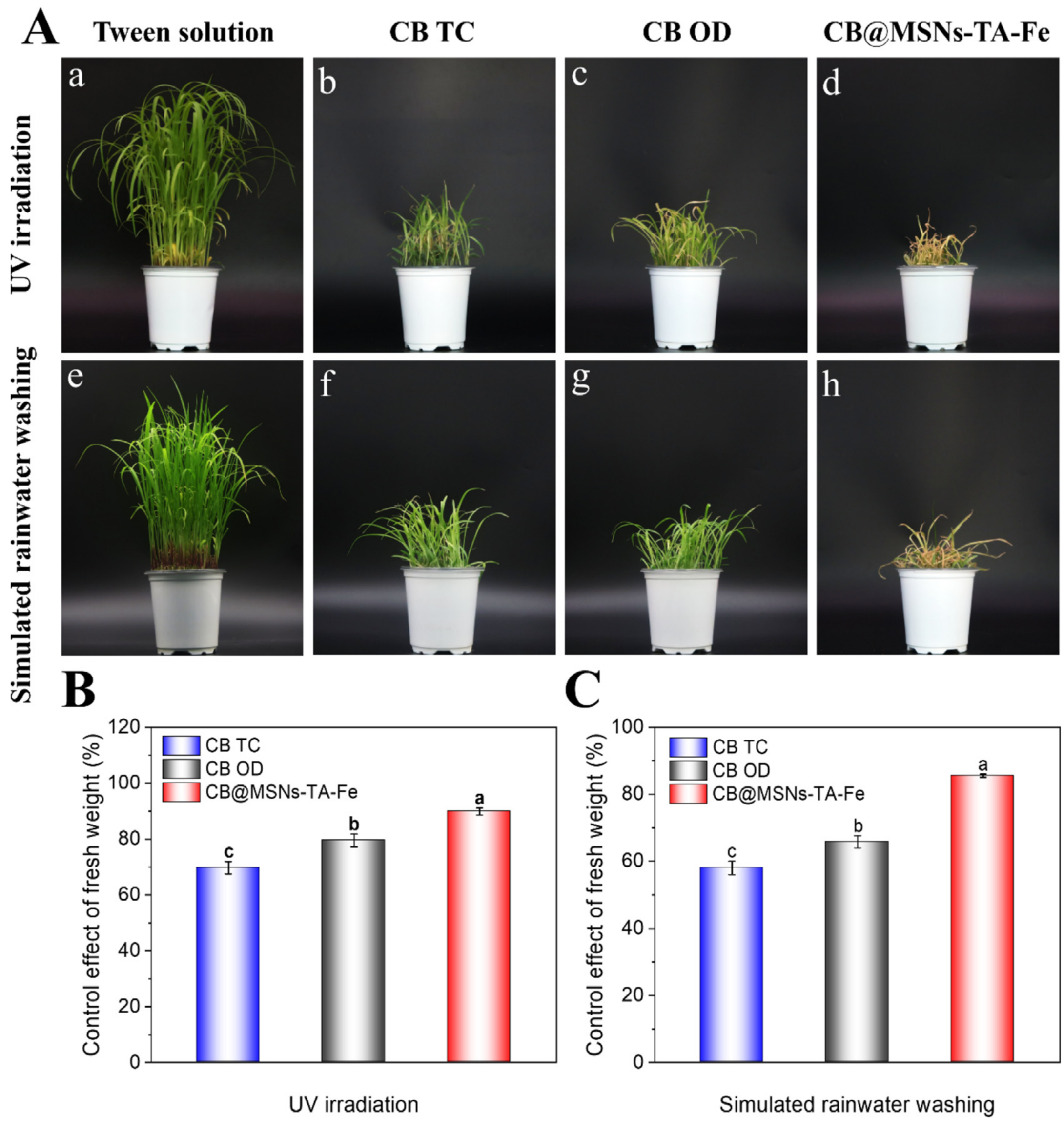

Fig. 5. High herbicidal activity of CB@MSNs-TA-Fe against barnyard grass. (A) Digital images of barnyard grass treated with 50 μg·mL^{-1} of the AIs of CB@MSNs-TA-Fe, CB TC, and CB OD under UV irradiation (a-d) and simulated rainwater washing (e-h) after 14 days. The corresponding control efficacies against barnyard grass under (B) UV irradiation and (C) simulated rainwater washing. Data were expressed as mean ± standard error of the mean (SE) for all experiments. Different lowercase letters indicate statistically significant differences ($P < 0.05$).

assessed, utilizing adult zebrafish as a model non-target species. As shown in Fig. 7, even at the maximum concentration of 1600 μg·mL^{-1} for MSNs-TA-Fe, the survival rate remains 100 % for zebrafish, thus confirming its excellent biosafety for aquatic organisms. Furthermore, we also evaluated the impact of the carrier material on soil organisms. **Fig. S8** indicates that all earthworms survive following a 7-day exposure to various concentrations of MSNs-TA-Fe, showing that the nano-carrier did not pose adverse effects on soil organisms. Collectively, the developed nano-carrier demonstrates high biosafety for plants, aquatic organisms, and soil organisms, rendering it highly suitable for application in herbicide nanoformulations.

Conclusions

In this study, a highly leaf-adhesive and anti-UV herbicide nanoformulation, CB@MSNs-TA-Fe, is successfully constructed for improving herbicidal activity based on metal phenolic network-coated functionalized mesoporous silica loaded with CB. The release rate of CB within CB@MSNs-TA-Fe under acidic conditions is higher than that under alkaline and neutral conditions. Moreover, the TA-Fe coating enables CB@MSNs-TA-Fe with markedly enhanced photostability, foliar adhesion, and flush-resistance performance on hydrophobic blades, thus significantly improving the utilization efficiency of AIs. The CB@MSNs-TA-Fe exhibits higher herbicidal activity against barnyard grass than CB TC and CB OD under UV irradiation or simulated rainwater scouring. The MSNs-TA-Fe nano-carrier, demonstrated to be biosafe for rice, zebrafish, and earthworms, revealing its potential as an eco-friendly herbicide delivery system. Overall, the developed herbicide nanoformulations, characterized by high foliar adhesion and anti-UV properties, reveal substantial potential in the management of malignant weeds, offering an effective, secure, and sustainable solution.

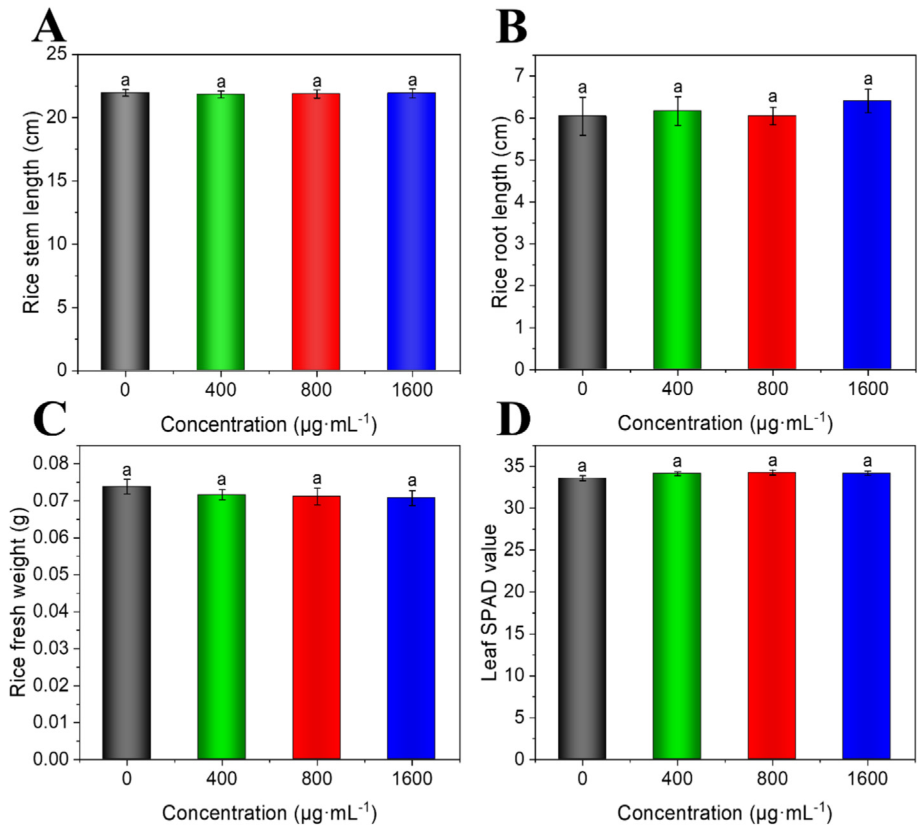

Fig. 6. Biosafety evaluation of MSNs-TA-Fe on rice growth. The effects of MSNs-TA-Fe at different concentrations on the (A) stem length, (B) root length, (C) fresh weight, and (D) SPAD value of rice seedlings after 7 days of treatments. Data were expressed as mean ± standard error of the mean (SE) for all experiments. Different lowercase letters indicate statistically significant differences ($P < 0.05$).

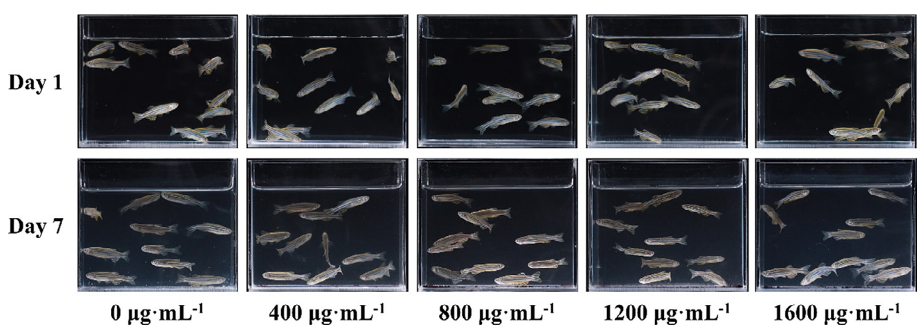

Fig. 7. Biosafety evaluation of MSNs-TA-Fe on aquatic organisms. Digital photo of zebrafish in tap water added with the pesticide carrier (MSNs-TA-Fe) at different concentrations. The zebrafish exposed to MSNs-TA-Fe nanoparticles at varying concentrations demonstrated a 100% survival rate.

Materials and methods

Additional experimental details are described in the supplementary materials.

CRediT authorship contribution statement

Dongdong Li: Performed experiments, Analyzed the data, Wrote the paper, Commented on the manuscript. **Jianan Li**: Performed experiments, Commented on the manuscript. **Hao Li**: Performed experiments, Commented on the manuscript. **Zhendong Bai**: Performed experiments, Commented on the manuscript. **Chujian Ma**: Performed experiments, Commented on the manuscript. **Haodong Bai**: Performed experiments, Commented on the manuscript. **Dingfeng Luo**: Performed experiments, Commented on the manuscript. **Zuren Li**: Designed the experiments, Analyzed the data, Wrote the paper, Commented on the manuscript. **Lianyang Bai**: Designed the experiments, Analyzed the data, Commented on the manuscript.

Compliance with ethics requirement

For studies that do not contain studies with human or laboratory animal subjects. All experimental materials for this study were collected in China, but did not cause the species to be threatened or endangered.

Declaration of competing interest

The authors declare that they have no known competing financial interests or personal relationships that could have appeared to influence the work reported in this paper.

Acknowledgements

This work was supported by the National Key Research and Development Program of China (2023YFD1400500), the China Agriculture Research System of MOF and MARA (CARS-16-E19), Natural Science Foundation of Hunan Provence (2024JJ1005, 2024JJ2036) and Hunan Agriculture Research System (2022-31), and Aid Program for Science and Technology Innovative Research Team in Higher Educational Institutions of Hunan Province (202301), and Scientific-Innovative of Hunan Agricultural Sciences and Technology (2023CX115).

Appendix A. Supplementary material

Supplementary data to this article can be found online at https://doi.org/10.1016/j.jare.2024.12.034.

References

[1] Zhao P, Yuan W, Xu C, Li F, Cao L, Huang Q. Enhancement of spirotetramat transfer in cucumber plant using mesoporous silica nanoparticles as carriers. J Agric Food Chem 2018;66:11592–600.
[2] Wan M, Zhang Y, Hong T, Cui J, Zhao Y, Wang Z. Degradable ZIF-8/silica carriers with accropode-like structure for enhanced foliar affinity and responsive pesticide delivery. Chem Eng J 2024;489:151301.
[3] Chen L, Huang J, Chen J, Shi Q, Chen T, Qi G, et al. Halloysite nanotube-based pesticide formulations with enhanced rain erosion resistance, foliar adhesion, and insecticidal effect. ACS Appl Mater Interfaces 2022;14:41605–17.
[4] Singh R, Shukla A, Kaur G, Girdhar M, Malik T, Mohan A. Systemic analysis of glyphosate impact on environment and human health. ACS Omega 2024;9:6165–83.
[5] Teng G, Chen C, Ma X, Mao H, Yuan X, Xu H, et al. Spherical assembly of halloysite clay nanotubes as a general reservoir of hydrophobic pesticides for pH-responsive management of pests and weeds. Small 2024:2402921.
[6] Deng X, Zhao P, Xie Y, Bai L. Self-assembled sphere covalent organic framework with enhanced herbicidal activity by loading cyhalofop-butyl. J Agric Food Chem 2023;71:1417–25.
[7] Xu Y, Xu C, Huang Q, Cao L, Teng F, Zhao P, et al. Size effect of mesoporous silica nanoparticles on pesticide loading, release, and delivery in cucumber plants. Appl Sci 2021;11(2):575.
[8] Deng X, Li J, Yi J, Lian R, Zhang Z, Li J, et al. A pH-responsive MOF-functionalized hollow mesoporous silica controlled herbicide delivery system exhibits enhanced activity against ACCase-herbicide-resistant weeds. Pest Manag Sci 2023;79:5237–49.
[9] Nel A, Xia T, Mädler L, Li N. Toxic potential of materials at the nanolevel. Science 2006;311:622–7.
[10] Singh G, Ramadass K, Sooriyakumar P, Hettithanthri O, Vithange M, Bolan N, et al. Nanoporous materials for pesticide formulation and delivery in the agricultural sector. J Control Release 2022;343:187–206.
[11] Dong J, Liu X, Chen Y, Yang W, Du X. User-safe and efficient chitosan-gated porous carbon nanopesticides and nanoherbicides. J Colloid Interface Sci 2021;594:20–34.
[12] Deng X, Zhao P, Zhou X, Bai L. Excellent sustained-release efficacy of herbicide quinclorac with cationic covalent organic frameworks. Chem Eng J 2021;405:126979.
[13] Song Y, Li Y, Xu Q, Liu Z. Mesoporous silica nanoparticles for stimuli-responsive controlled drug delivery: advances, challenges, and outlook. Int J Nanomed 2017;12:87–110.
[14] Liu T, Zhang M, Liu W, Zeng X, Song X, Yang X, et al. Metal ion/tannic acid assembly as a versatile photothermal platform in engineering multimodal nanotheranostics for advanced applications. ACS Nano 2018;12:3917–27.
[15] Dong J, Chen W, Qin D, Chen Y, Li J, Wang C, et al. Cyclodextrin polymer-valved MoS_2-embedded mesoporous silica nanopesticides toward hierarchical targets via multidimensional stimuli of biological and natural environments. J Hazard Mater 2021;419:126404.
[16] Allais M, Meyer F, Ball V. Multilayered films made from tannic acid and alkaline phosphatasewith enzymatic activity and electrochemical behavior. J Colloid Interface Sci 2018;512:722–9.
[17] Chakrabarty T, Pérez-Manríquez L, Neelakanda P, Peinemann K-V. Bioinspired tannic acid-copper complexes as selective coating for nanofiltration membranes. Sep Purif Technol 2017;184:188–94.
[18] Guo J, Suma T, Richardson JJ, Ejima H. Modular assembly of biomaterials using polyphenols as building blocks. ACS Biomater Sci Eng 2019;5:5578–96.
[19] Wan M, Hong T, He G, Zhao Y, Sun L. Multifunctional hollow silica carriers with spiny structure for enhanced foliar adhesion and triple-responsive pesticide delivery. Chem Eng J 2023;475:146461.
[20] Dong J, Chen W, Feng J, Liu X, Xu Y, Wang C, et al. Facile, Smart, and degradable metal–organic framework nanopesticides gated with Fe^{III}-tannic acid networks in response to seven biological and environmental stimuli. ACS Appl Mater Interfaces 2021;13:19507–20.
[21] Cheng M, Yan X, Cui Y, Han M, Wang X, Wang J, et al. An eco-friendly film of pH-responsive indicators for smart packaging. J Food Eng 2022;321:110943.
[22] Vanitha J, Amudha K, Mahendran R, Srinivasan J, Kumari RU. A review on molecular marker analysis for yield and its component traits under water stress and zinc deficiency tolerance in rice. Int J Curr Microbiol Appl Sci 2019;8:1013–8.
[23] Karim R, Man A, Sahid I. Weed problems and their management in rice fields of malaysia: an overview. Weed Biol Manag 2004;4:177–86.
[24] Chen G, Wang Q, Yao Z, Zhu L, Dong L. Penoxsulam-resistant barnyardgrass (*Echinochloa crus-galli*) in rice fields in China. Weed Biol Manag 2016;16:16–23.
[25] Yang X, Zhang Z, Gu T, Dong M, Peng Q, Bai L, et al. Quantitative proteomics reveals ecological fitness cost of multi-herbicide resistant barnyardgrass (*Echinochloa crus-galli L.*). J Proteomics 2017;150:160–9.
[26] Zhang Z, Cao J, Gu T, Yang X, Peng Q, Bai L, et al. Co-planted barnyardgrass reduces rice yield by inhibiting plant above- and belowground-growth during post-heading stages. Crop J 2021;9:1198–207.
[27] Wu J, Wang K, Zhang Y, Zhang H. Determination and study on dissipation and residue determination of cyhalofop-butyl and its metabolite using HPLC-MS/MS in a rice ecosystem. Environ Monit Assess 2014;186:6959–67.
[28] Li Z, Zhang X, Wang Y, Zheng Z, Zhang C, Wu T, et al. Improved method to characterize leaf surfaces, guide adjuvant selection, and improve glyphosate efficacy. J Agric Food Chem 2023;71:1348–59.
[29] Sanyal D, Bhowmik P, Reddy K. Influence of leaf surface micromorphology, wax content, and surfactant on primisulfuron droplet spread on barnyardgrass (*Echinochloa crus-galli*) and green foxtail (*Setaria viridis*). Weed Sci 2006;54:627–33.
[30] Zhu G, Wu G, Zhao L, Wu H. Photo-degradation of cyhalofop-butyl and its metabolite (acid) in various aqueous solutions. Chin J Pestic Sci 2003;5:65–70.
[31] Zhao W, Huang S, Li M, Ouyang X, Ling J. Efficient delivery of fucoxanthin using alginate oligosaccharide-coated mesoporous silica. Mater Today Commun 2024;38:108564.
[32] Guo J, Ping Y, Ejima H, Alt K, Meissner M, Richardson J, et al. Engineering multifunctional capsules through the assembly of metal–phenolic networks. Angew Chem, Int Ed 2014;53:5546–51.
[33] Kaur J, Tikoo K. Evaluating cell specific cytotoxicity of differentially charged silver nanoparticles. Food Chem Toxicol 2013;51:1–14.
[34] Wang C, Qiao K, Ding Y, Liu Y, Niu J, Cao H. Enhanced control efficacy of spinosad on corn borer using polylactic acid encapsulated mesoporous silica nanoparticles as a smart delivery system. Int J Biol Macromol 2023;253:126425.
[35] Sing K. Adsorption methods for the characterization of porous materials. Adv Colloid Interface Sci 1998;76–77:3–11.
[36] Xu C, Cao L, Zhao P, Zhou Z, Cao C, Li F, et al. Emulsion-based synchronous pesticide encapsulation and surface modification of mesoporous silica nanoparticles with carboxymethyl chitosan for controlled azoxystrobin release. Chem Eng J 2018;348:244–54.
[37] Jing H, Huang X, Jiang C, Wang L, Du X, Ma C, et al. Effects of tannic acid on the structure and proteolytic digestion of bovine lactoferrin. Food Hydrocoll 2021;117:106666.
[38] Cao L, Zhang H, Zhou Z, Xu C, Shan Y, Lin Y, et al. Fluorophore-free luminescent double-shelled hollow mesoporous silica nanoparticles as pesticide delivery vehicles. Nanoscale 2018;10:20354–65.
[39] Liang Y, Guo M, Fan C, Dong H, Ding G, Zhang W, et al. Development of novel urease-responsive pendimethalin microcapsules using silica-IPTS-PEI as controlled release carrier materials. ACS Sustain Chem Eng 2017;5:4802–10.
[40] Wang J, Gao P, Yang X, Wang T, Wang J, Huang C. Real-time imaging of intracellular drug release from mesoporous silica nanoparticles based on fluorescence resonance energy transfer. J Mater Chem B 2014;2:4379–86.
[41] Abdelrahman TM, Qin X, Li D, Senosy IA, Mmby M, Wan H, et al. Pectinase-responsive carriers based on mesoporous silica nanoparticles for improving the translocation and fungicidal activity of prochloraz in rice plants. Chem Eng J 2021;404:126440.
[42] Liang Y, Song J, Dong H, Huo Z, Gao Y, Zhou Z, et al. Fabrication of pH-responsive nanoparticles for high efficiency pyraclostrobin delivery and reducing environmental impact. Sci Total Environ 2021;787:147422.
[43] Tang J, Tong X, Chen Y, Wu Y, Zheng Z, Kayitmazer AB, et al. Deposition and water repelling of temperature-responsive nanopesticides on leaves. Nat Commun 2023;14:6401.